This is the accepted manuscript made available via CHORUS. The article has been published as:

Charge-induced phase transition in encapsulated math xmlns="http://www.w3.org/1998/Math/MathML">mrow>mi>Hf/mi>msub>mi>Te/mi>mn>2/mn>/msub>/mrow>/math> nanoribbons

Derek Popple, Mehmet Dogan, Tony Vo Hoang, Scott Stonemeyer, Peter Ercius, Karen C. Bustillo, Marvin Cohen, and Alex Zettl

Phys. Rev. Materials **7**, L013001 — Published 4 January 2023

DOI: 10.1103/PhysRevMaterials.7.L013001

Charge-induced phase transition in encapsulated $HfTe_2$ nanoribbons

Derek Popple[1-4], Mehmet Dogan[2,3], Tony Vo Hoang[1], Scott Stonemeyer[1-4], Peter Ercius[5], Karen C. Bustillo[5], Marvin Cohen[2,3], Alex Zettl[2-4]*

1. Department of Chemistry, University of California Berkeley, Berkeley, CA 94720
2. Department of Physics, University of California Berkeley, Berkeley, CA 94720
3. Materials Sciences Division, Lawrence Berkeley National Lab, 1 Cyclotron Road, Berkeley CA, 94720
4. Kavli Energy NanoScience Institute at the University of California at Berkeley and the Lawrence Berkeley National Laboratory, Berkeley, CA, 94720
5. National Center for Electron Microscopy, Molecular Foundry, Lawrence Berkeley National Lab, 1 Cyclotron Road, Berkeley CA, 94720

Abstract

Nanotube encapsulation is a powerful technique for coaxing solids into unconventional configurations. By synthesizing materials within the interior confines of hollow nanotubes, lower dimensional morphologies, such as one-dimensional chains or nanoribbons, are favored. We have used carbon nanotube encapsulation to realize ultra-narrow, atomically precise $HfTe_2$ nanoribbons. A local, electron-beam-stimulated transition from the metallic 1T phase to the previously unreported semiconducting 1H phase is observed. We study computationally how charging can drive the phase transition and the stability of the different atomic configurations.

Introduction

Reducing the size of a material to the nanoscale can result in properties drastically different from those of the bulk, parent material. Nanostructuring can increase the surface area to volume ratio, promote the display of reactive edge terminations, and modify the electronic structure. [1–5] For materials like the carbon-based graphene nanoribbons, sophisticated organic chemistry enables the bottom-up synthesis of

atomically precise structures with desired width and edge configuration. [6] However, for inorganic materials such as the transition metal dichalcogenides (TMDs), the nature of the ionocovalent bonds hinders such designer synthesis. Nevertheless, creating lower dimensional forms of the TMDs such as nanoribbons is of great interest, as this would allow access to band gap tuning and new edge chemistries, and facilitate associated applications. [7–10] Several attempts have been made to reduce the dimensionality of TMDs towards more one-dimensional nanoribbons. Top-down techniques, where the two-dimensional parent material is cut into strips have been realized through chemical unzipping techniques [11,12] as well as with lithographic strategies employing electron [13] or ion beams [14]. Although these strategies can yield rudimentary nanoribbons, the widths of the ribbons are usually too large to enable quantum confinement effects, and the ribbons typically have poorly-defined edges that compromise the electronic properties. [15] Some bottom-up techniques have also been demonstrated via nanowire-to-nanoribbon conversion, [16] reaction of patterned precursors on substrates, [17] and molecular beam epitaxy. [18] Such techniques may allow the possibility of fabricating nanoribbons in parallel, but the requirements of lithographic strategies or stringent ultrahigh vacuum molecular beam epitaxy conditions diminish the scalability of these techniques.

Alternatively, hollow nanotubes can be exploited as nanoscale reaction vessels to access new low-dimensional morphologies that would otherwise be difficult to realize through unassisted bottom-up synthesis. As the new material grows within the nanotube, steric hinderance imposed by the nanotube walls limits the growth in the radial directions while growth in the coaxial direction is uninhibited. This can drive the synthesis towards more one-dimensional morphologies such as chains or nanoribbons, where the lateral dimension of the internal nanostructure is dictated by the inner diameter of the nanotube. By pre-selecting nanotubes of a given inner diameter, the lateral dimensions of the desired material can be dialed in. [19]

Nanotube encapsulation has been demonstrated for a large number of materials, employing both carbon nanotubes (CNTs) and boron nitride nanotubes (BNNTs) as hosts. [20–26] The method was first

applied to the synthesis of TMDs with the demonstration of MoS_2@CNT. [27] In that work, the CNTs were filled with aqueous precursors and annealed under reducing, S-rich conditions to produce the MoS_2 nanoribbons. WS_2 nanoribbons have been similarly produced, [28] and more recently TaS_2 nanoribbons with interesting periodic superstructure have been created, [29] but little else has been reported. It is apparent that encapsulation of other compositions of TMD nanoribbons beyond the Group IV transition metals (Mo and W) and disulfides could yield a wealth of interesting properties, and these materials warrant investigation.

Here we report the first synthesis of $HfTe_2$ nanoribbons, achieved via chemical vapor transport within CNTs, and characterize the nanoribbons via high angle annular dark field scanning transmission electron microscopy (HAADF-STEM). We find that stimulation from the STEM electron beam can drive a local phase transition from the 1T phase to the previously unreported (for $HfTe_2$) 1H polymorph. We examine theoretically the stability and electronic structure of $HfTe_2$ nanoribbons and find that 1T nanoribbons are metallic while 1H nanoribbons are semiconducting. We examine the role charging plays in driving the structural phase transition.

Results and Discussion

The nanoribbons are synthesized via chemical vapor transport within multi-wall carbon nanotubes similar to a previously published procedure. [29] Bright field TEM shows the nanoribbon as well as the walls of the encapsulating nanotubes (Fig. S1). Nanoribbons were observed with widths between 1.37 and 7.27 nm and with lengths usually greater than 100 nm (Fig. S2). The nanoribbons are usually monolayer in thickness, although for the larger inner-diameter nanotubes, multi-layer ribbons are possible (Fig. S3). The edge on view of the multilayered ribbons shows the sandwich structure common to all TMDs as well as the expected interlayer separation of ~0.6 nm. Elemental analysis via energy dispersive X-ray spectroscopy (EDS) shows the presence of both hafnium and tellurium (Fig S4); the full EDS spectrum is available in the Supplemental Information (SI) (Figs. S5/S6). For mapping, custom energy ranges are

defined to construct maps of the Hf $L_{\beta 2}$ and Te $L_{\alpha 1}$ transitions. These specific transitions are used to avoid overlap of other element edges in the sample such as iodine (transport agent) or copper (TEM grid). Experimental details on nanoribbon synthesis as well as additional TEM images and EDS spectra are included in the Supplemental Material [30] (see, also, references [19,25,31–40] therein).

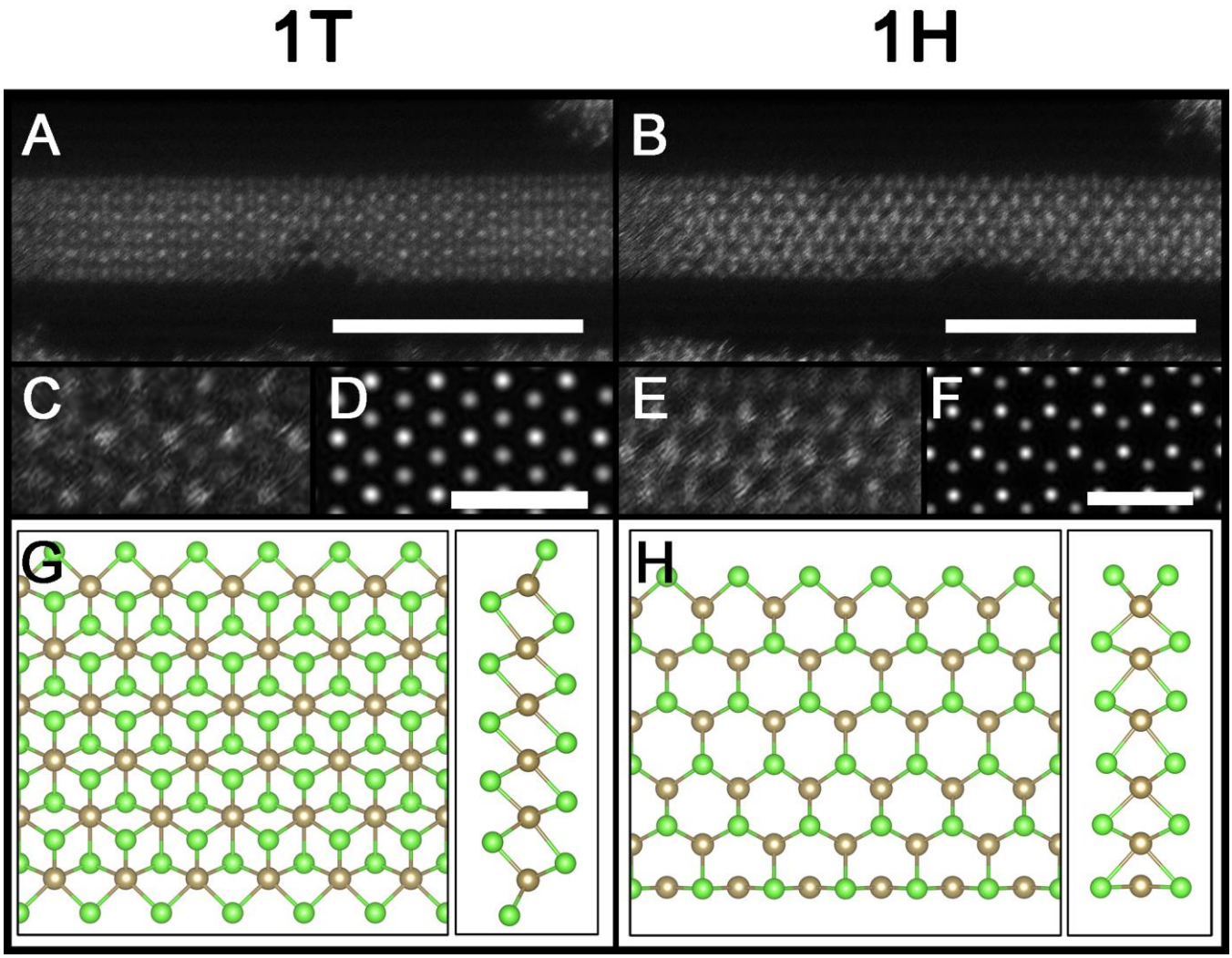


Figure 1. STEM imaging and image simulations of the 1T and 1H phase of $HfTe_2$@CNT. HAADF-STEM images show the basal plane of the 1T (A) and 1H (B) phase of the same region of a single 2mm wide nanoribbon. The encapsulating carbon nanotube is a four-walled tube with an inner diameter of 2.2 nm. Scalebar A, B: 5nm. Higher magnification STEM images show the filled honeycomb structure indicative of the 1T phase (C) and the empty honeycomb structure indicative of the 1H phase (E). STEM image simulations of each phase (D, F) allow a comparison of the observed

structures and the calculated structures of each phase. Scalebar C-F: 1nm. Atomic models for each phase (G, H) show an ideal depiction of the basal plane and edge structure of each phase with a width of 6 unit cells, obtained through first-principles relaxation (see text).

Figure 1 presents experimental structural characterization. The nanoribbons are imaged via HAADF-STEM, which gives approximate Z contrast allowing resolution of the atomic lattice while making the carbon nanotube nearly transparent. Fig. 1A presents a view of the basal plane which shows the filled hexagonal pattern typical of the 1T phase of TMDs. Due to the similar atomic numbers of Hf and Te, there is little contrast between the elements, although a slight difference in intensity can be seen between nearest neighbors. Typically, atomic perfection is maintained along the nanoribbon edges. As a counterexample, on the bottom edge of the nanoribbon of Fig. 1A, an edge defect with several missing atoms is observed. A higher magnification image of the same ribbon is shown in Fig. 1C alongside a STEM image simulation in Fig. 1D. Despite the experimental difficulties associated with monolayer thickness samples and thermal vibrations, exceptional agreement is found between the experimental image of Fig. 1C and simulation of Fig. 1D. In Fig. 1C it is possible to make out the trigonal arrangement of atoms expected from the trigonal (1T) unit cell of $HfTe_2$. A schematic of the 1T structure viewed perpendicular to the basal plane is shown in Fig. 1G, with an inset showing the edge on view of the structure.

We find that, upon stimulation from the electron beam during HAADF-STEM imaging, the $HfTe_2$ nanoribbon can undergo a structural phase transition from the nominal 1T phase with a "filled" hexagonal pattern to a different polymorph with an "unfilled" hexagonal pattern. This unfilled pattern is the characteristic signature of the 1H phase. It should be noted that while this is typically referred to as the 2H phase in the literature when discussing the parent 2D material, 1H is the proper nomenclature here since the encapsulated sample is a monolayer. A video of the dynamics is provided in the Supplemental Materials (Movie S1), obtained through successive rapid acquisitions in the STEM microscope. [30] Due

to the lower resolution needed to capture the movie at a higher framerate, it is not possible to resolve the lattice at atomic resolution, but one readily observes the transition from the 1T to 1H phase, as well as a transition back to the 1T phase. While the exact timescale of the transition is difficult to determine due to the complex dynamics of the ribbon under constant electron beam exposure, based on the frame rate of ~1 Hz, the phase change is observed on the order of 10 s.

A HAADF-STEM micrograph of the basal plane (Fig. 1B) shows the unfilled hexagonal pattern typical of the 1H phase at atomic resolution. Note that the same defect on the bottom of the ribbon is present in Fig. 1B as in Fig. 1A, which serves as a position marker (drift of the microscope has shifted the imaging window slightly to the right. A higher magnification image of the 1H transformed nanoribbon is given in Fig. 1E alongside a STEM image simulation of the 1H phase (Fig. 1F). These again show agreement between the relative spacing and orientations of the atoms in the experimental and simulated 1H images. A schematic of the structure with an inset of the edge-on view is given in Fig. 1H. We note that this is the first report of the 1H phase in $HfTe_2$ (as the 2H phase has not, to our knowledge, been previously reported for bulk or monolayer form of $HfTe_2$).

We now turn to a theoretical investigation of $HfTe_2$ nanoribbons. Using first-principles calculations, we examine the stability of the different phases, the transitions between the phases, and the role of charging in driving the transitions. We demonstrate that the 1T phase is metallic while the 1H phase is semiconducting, meaning that the directed structural phase transition is also associated with a metal-semiconductor transition.

First, we optimize single layer $HfTe_2$ in the 1T and 1H phases and find that the 1H phase is 0.40 eV/$HfTe_2$ higher in total energy. The lattice parameters for the 1T and 1H phases are determined as 3.95 and 3.89 Å, respectively. Combining single layers of 1T (1H) phase in the most energetically favorable way leads to the multiple layer 1T (2H) phase. The dependence of the energetics on the number of layers turns out to be weak (Fig. 2A) and therefore is not expected to drive the phase transition.

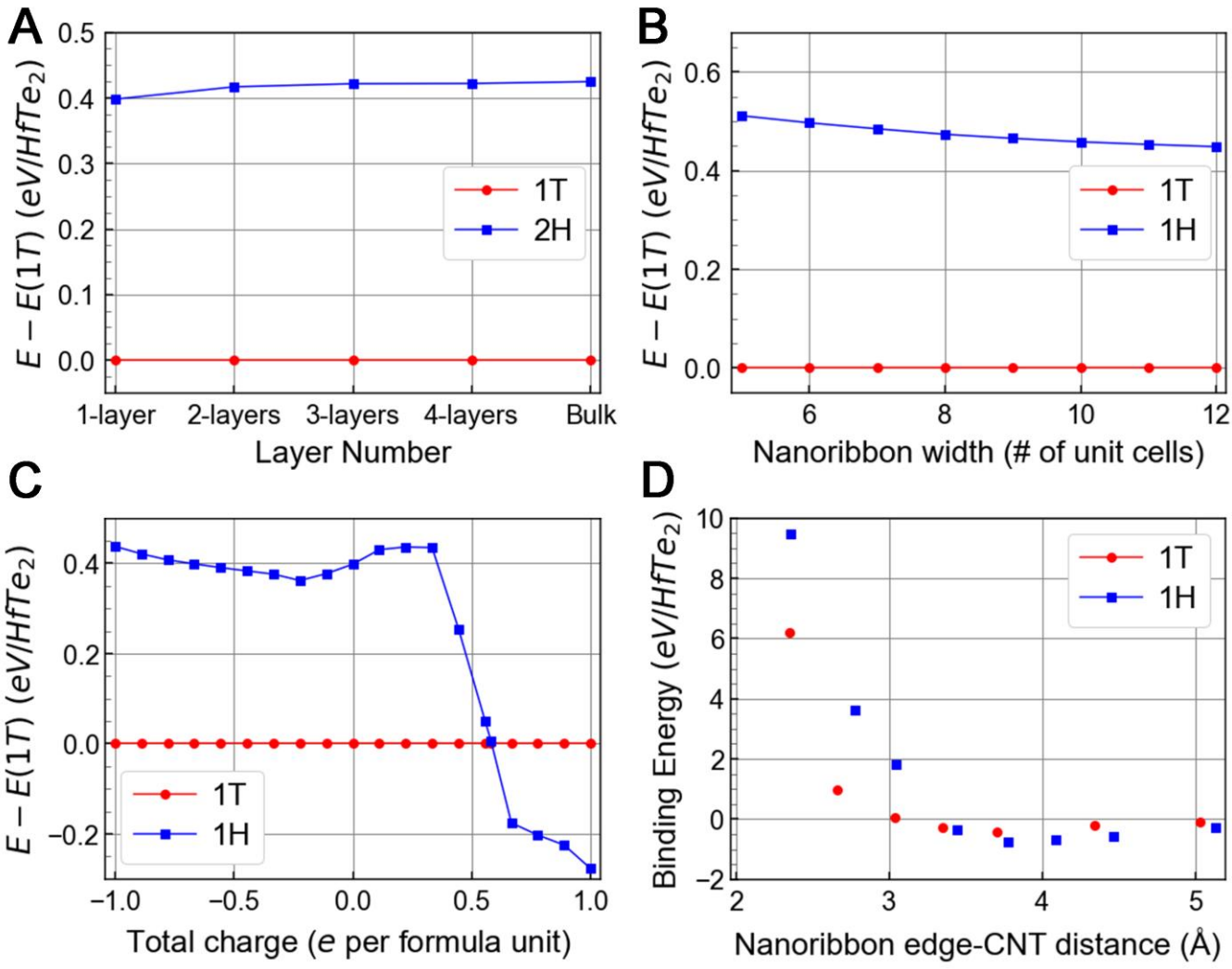


Figure 2. Energetics of $HfTe_2$ phases. Energetic comparisons between the three main phases of $HfTe_2$. (A,B,C) Total energy of the phases with respect to 1T examined as a factor of (A) number of layers, (B) nanoribbon (NR) width, and (C) total charge. (D) For NRs encapsulated in carbon nanotubes (CNTs), the binding energy of each $HfTe_2$ configuration as a function of distance between the NR edge and the CNT inner walls.

In principle, edge reconstructions in nanoribbons may significantly change the energetics relevant to a phase transition. To explore this possibility, we compute relaxed configurations of $HfTe_2$ nanoribbons with widths of 5- to 12-unit cells (u.c.). As zig-zag nanoribbons are exclusively observed in the experiment (*i.e.* edges along the [100] direction), we only simulate zig-zag nanoribbons. For simplicity, we focused

on stoichiometric ribbons, where the Te:Hf ratio is 2:1. In the case of the 1H phase, the natural choice is to terminate one edge with Hf and the other edge with Te_2 (Fig. 1G). In the case of the 1T phase, a few choices of termination are possible, e.g., where one edge is terminated with Hf and the other with Te_2 with 2×1 relaxations. We find that lowest energies are obtained when both edges are terminated with Te_1 (Fig. 1H). Typical examples of these optimized NRs are shown in Figs. 1G-H for 6 u.c. wide nanoribbons, and edge relaxations are qualitatively the same for all other widths. In Fig. 2B, we present the energetics of NRs as a function of width and find that the 1H phase becomes slightly more unfavorable compared to the 1T phase as the NR is made narrower. We note that our simulated edges have a remarkable resemblance to the edges observed in the STEM images in Fig. 1. The lower edge in Fig, 1A and both edges in Fig. 1B match with their theoretical counterparts in Figs. 1G-H, as can be verified by inspection. The upper edge in Fig. 1A appears to differ from the theoretical edge in Fig. 1G, which indicates that that NR may not be stoichiometric. However, for all edge constructions we studied for the 1T NRs, we found the 1H NRs to lie at higher energies for a given width. Therefore, we conclude that finite size effects in NRs do not account for the observed phase transition.

As an obvious candidate for an effect that might lead the 1T and 1H phases to be degenerate, we investigate charge transfer (first in the absence of any external charging source, such as a TEM electron beam), as internal charging is known to be significant in some CNT encapsulated systems. [26] We relax both phases in 3×3 supercells and add or removed integer numbers of electrons. The resulting dependence of energy on charge is presented in Fig. 2C, which demonstrates that an electron rich environment does not stabilize the 1H phase but removing electrons from the system does. The exact value of added charge that makes the two phases degenerate is 0.58 $|e|$ per $HfTe_2$. Hence, if encapsulation by a CNT removes electrons from the NR, it may favor the experimentally observed phase transition.

To check whether this hypothesis of electron removal holds, we set up model $HfTe_2$–CNT systems where armchair CNTs are constrained to match the $HfTe_2$ lattice constants, and no further relaxations are performed. In this set of calculations, we use 5, 6 and 7 u.c. wide NRs and (m, m) CNTs with $m =$

16, 17, 18, and 19. The optimized lattice constant of these CNTs is 2.46 Å, which is close to 2/3 of the $HfTe_2$ lattice constants. Therefore, we generate simulation cells with 3 u.c. of CNT and 2 u.c. of NRs, leading to 6.6% and 5.1% tensile strains on CNTs for the 1T and 1H phases, respectively. To compensate for this tensile strain in the CNT axis, we decrease their diameters proportionally, using the Poisson ratio of 0.2, based on previous studies. [41–46] In Fig. 2D, the resulting binding energies, defined as the total energy of the CNT+NR system minus the total energies of the CNT and NR systems separately, are presented as a function of the distance between the CNT and the edge of the NR. Although these values are a result of unrelaxed model calculations, they behave as expected, becoming negative (attractive) or positive (repulsive) based on the distance between the CNT and the NR edge. When this distance is larger than ~3.2 Å, both phases become stable, and the 1H phase is stabilized slightly more than the 1T phase for comparable NR–CNT distances.

With these systems set up, we next compute the charge transfer between the CNT and the nanoribbon. First, we define charge redistribution as $\Delta\rho(r,\phi,x) = \rho(\text{CNT+NR}) - \rho(\text{CNT}) - \rho(\text{NR})$, where the $\Delta\rho$ is expressed in terms of cylindrical coordinates with x being the coordinate along the periodic direction. In Fig. S6, we show the isosurface plots of $\Delta\rho$ for 5 u.c. wide nanoribbons of both phases. [30] It is observed in these plots that the nanoribbons lose electrons to the CNTs, which is also the case for other structures we inspected. To quantify the aggregate electron transfer, we plot $\int_0^{2\pi}\int_0^{a} r\Delta\rho(r,\phi,x)dxd\phi$ as a function of r (where a is the lattice parameter) and integrate the result up to the value of r at which the integral changes sign. For the seven most strongly bound structures with a CNT–nanoribbon distance between 3.2 and 4.6 Å, we find the charge transfer to be in the range of 0.21 to 0.40 *e* per $HfTe_2$. These values are smaller than the 0.58 *e* per $HfTe_2$ required to reach equality between the two phases, but it demonstrates that internal charging is a significant contributor towards driving the phase transition.

Experimentally, we observe the transition from 1T to 1H during active HAADF-STEM imaging, where the external STEM electron beam is locally irradiating the sample. The "external" charging effects under such circumstances are complex and difficult to quantify, but, contrary to simple intuition, the STEM electron beam can actually positively charge the sample. [47] Hence, internal and external charging can conspire to make the 1H phase energetically more favorable (Fig. 2C) and this likely drives the transition.

The fact that $HfTe_2$ nanoribbons are intrinsically charged inside CNTs has implications for the stability and possible phase changes of the nanoribbons, even without an external electron beam present. To explore these implications, we conduct a transition state study using the nudged elastic band (NEB) method. First, we compute the energy barrier between the 1T and 1H phases when the phase transition occurs simultaneously in the whole film, for both the neutral films and the films charged to reach degeneracy between the phases (0.58 $|e|$ per $HfTe_2$). Because the NEB method requires a fixed u.c., we use slightly modified initial and final states in which the lattice constants are both set to 3.92 Å. We find that internal charging reduces the energy barrier from 0.56 eV (forward) and 0.16 eV (backward) to 0.13 eV in both directions (Fig. 3A). The transition state as well as the initial and final states are presented in Fig. 3B for the neutral case (the charged case is similar). This indicates that the intrinsically positively charged films should be more amenable for this phase transition.

The approximation of an infinite slab simultaneously going through a phase transition does not closely correspond to real materials in which there are phase domains and boundaries. To investigate a representative case for phase boundary dynamics, we choose the shift of a zig-zag domain wall between the two phases by one u.c. In Fig. 3C, the transition barrier is shown for both the neutral and charged cases: 0.36 eV and 0.19 eV, respectively. To construct the phase boundary, we generate supercells with 7, 9 and 11 units of each phase along the x-direction. Keeping the coordinates of the center unit of each domain fixed to their infinite slab values, we relax all the remaining coordinates. The two domain walls that occur in such a calculation are not equivalent, so it is only possible to refer to their total energies,

defined as the energy of the full supercell calculation of size $2n$ minus the energies of n 1T and n 1H unit cells.

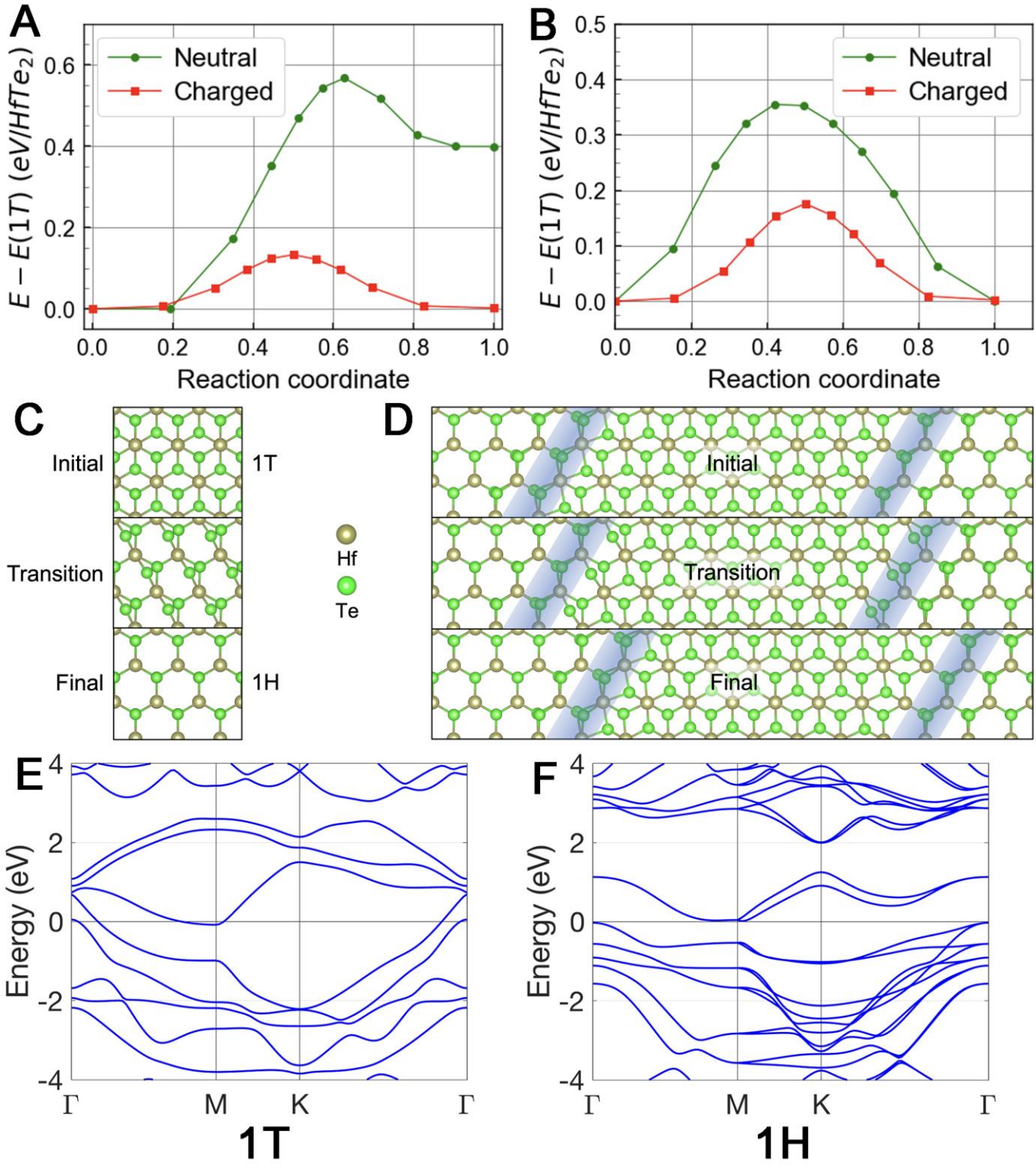


Figure 3. Phase transition mechanisms in HfTe$_2$@CNT. (A) Energy barrier for the transition path between the 1T and 1H phases for single layer HfTe$_2$ when all unit cells coherently go through the transition, plotted for both the neutral case and the case where the two phases are charged 0.58 |e| per

f.u. (B) The initial, transition and final states for the transition in (A). (C) Energy barrier for the shift of a zig-zag domain wall by 1 u.c. for single layer $HfTe_2$, plotted for both the neutral case and the case where the two phases are charged 0.58 $|e|$ per f.u. (D) The initial, transition and final states for the transition in (C). The band structures of (E) metallic 1T and (F) semiconducting 1H $HfTe_2$ single layers at the PBE level, with spin–orbit interaction included. The calculation in (F) greatly underestimates the bandgap; at the more accurate HSE06 hybrid functional calculation level, the indirect semiconducting gap of the 1H phase is 0.7 eV (see text). The Fermi level is set to 0 eV.

These double domain wall energies for $n = 7,9,11$ are 0.82, 0.80 and 0.79 eV, respectively. Because these values are close and the distortions around the domain boundaries are very localized (Fig. 3D), we conduct the NEB calculations using $n = 7$. For the charged case, the double domain wall energy is 0.57 eV for $n = 7$. Because this energy as well as the barrier is smaller for the charged case, it is expected to be more conducive to robust domain dynamics. The transition state for the domain wall shift is also shown in Fig. 3D for the neutral case (the charged case is similar), indicating that the displacements remain local during such a domain wall shift. We note that these transition barriers are an order of magnitude larger than the thermal energy provided around room temperature, further emphasizing the role of the electron beam in driving the transition.

Finally, we present the band structures of the monolayer phases in Fig. 3E/F, where the 1T phase of $HfTe_2$ is a metal and the 1H phase has a (greatly underestimated) gap of 0.04 eV at the PBE level. In order to determine more accurate band gaps, we use the HSE06 hybrid functional which has a record of success in predicting band gaps in similar TMD systems to within 10% error. [48] At the HSE level, the 1T phase remains a metal but the band gap of the 1H phase increases to 0.71 eV (indirect, Γ→M). Thus, and importantly, the charge-driven phase transition we observe in $HfTe_2$ nanoribbons represents not only a structural phase transition, but a concomitant electronic metallic to semiconducting phase transition as well.

Conclusion

In summary, chemical vapor transport and nanotube encapsulation have been used to synthesize $HfTe_2$ nanoribbons for the first time. The as-produced nanoribbons are in the (ground state) 1T metallic 1T phase, but a phase transition from 1T to the formerly unrealized semiconducting 1H phase can be driven *in-situ* via electron beam stimulation. First-principles calculations clarify the role size effects, edge effects, and internal and external charging play in the stability of the materials and driving the transition while revealing the electronic band structures. CNT encapsulation and internal charging make the 1H phase more competitive and lowers the barrier to phase transition dynamics. This work expands knowledge of how nanotube encapsulation can be used to synthesize nanoribbons of unconventional TMDs, especially for the ditelluride species. The charge-induced phase change from the 1T to the 1H polymorph suggests technological implications where electron beams could be used to specifically pattern local regions of different phases within a nanoribbon, creating, for example, tailored rectifying metal-semiconductor Schottky heterojunctions. [49]

Supplemental Material

See Supplemental Material at [URL will be inserted by publisher] for:

Details of synthesis of $HfTe_2$ nanoribbons, methods for STEM imaging and simulations, and computational details (PDF)

Movie of ribbon phase change via STEM (.mp4)

AUTHOR INFORMATION

Corresponding Author

* azettl@berkeley.edu

Acknowledgements

This work was primarily funded by the U.S. Department of Energy, Office of Science, Office of Basic Energy Sciences, Materials Sciences and Engineering Division under Contract No. DE-AC02-05-CH11231 within the van der Waals Heterostructures Program (KCWF16) which provided for design of the project, synthesis of the compounds, and TEM and STEM structural characterization. Additional support was provided by the U.S. Department of Energy, Office of Science, Office of Basic Energy Sciences, Materials Sciences and Engineering Division, under Contract No. DE-AC02-05-CH11231 within the sp2-Bonded Materials Program (KC2207) which provided for elemental mapping and structural stability calculations. Work at the Molecular Foundry (TEAM 0.5 and TitanX TEM) was supported by the U.S. Department of Energy, Office of Science, Office of Basic Energy Sciences, Materials Sciences and Engineering Division, under Contract No. DE-AC02-05-CH11231. Support was also provided by the National Science Foundation under Grant Nos. DMR-1807233, which provided for preparation of opened nanotubes, and DMR-1926004, which provided for theoretical calculations of the electronic structure. The charging and energy barrier calculations were supported by the U.S. Department of Energy, Office of Science, Office of Basic Energy Sciences, Materials Sciences and Engineering Division, under Contract No. DE-AC02-05-CH11231 within the Theory of Materials Program (KC2301). Computational resources were provided by the DOE at Lawrence Berkeley National Laboratory's NERSC facility and the NSF through XSEDE resources at NICS as well as TACC.

Notes

The authors declare no competing financial interest.

REFERENCES

[1] R. Van Hardeveld and F. Hartog, *The Statistics of Surface Atoms and Surface Sites on Metal Crystals*, Surface Science **15**, 189 (1969).

[2] K. S. Novoselov, A. K. Geim, S. V. Morozov, D. Jiang, M. I. Katsnelson, I. V. Grigorieva, S. V. Dubonos, and A. A. Firsov, *Two-Dimensional Gas of Massless Dirac Fermions in Graphene*, Nature **438**, 197 (2005).

[3] T. Li and G. Galli, *Electronic Properties of MoS_2 Nanoparticles*, J. Phys. Chem. C **111**, 16192 (2007).

[4] K. F. Mak, C. Lee, J. Hone, J. Shan, and T. F. Heinz, *Atomically Thin MoS_2: A New Direct-Gap Semiconductor*, Phys. Rev. Lett. **105**, 136805 (2010).

[5] S. Balasubramanyam, M. Shirazi, M. A. Bloodgood, L. Wu, M. A. Verheijen, V. Vandalon, W. M. M. Kessels, J. P. Hofmann, and A. A. Bol, *Edge-Site Nanoengineering of WS_2 by Low-Temperature Plasma-Enhanced Atomic Layer Deposition for Electrocatalytic Hydrogen Evolution*, Chem. Mater. **31**, 5104 (2019).

[6] J. Cai, P. Ruffieux, R. Jaafar, M. Bieri, T. Braun, S. Blankenburg, M. Muoth, A. P. Seitsonen, M. Saleh, X. Feng, et al., *Atomically Precise Bottom-up Fabrication of Graphene Nanoribbons*, Nature **466**, 7305 (2010).

[7] Y. Li, Z. Zhou, S. Zhang, and Z. Chen, *MoS_2 Nanoribbons: High Stability and Unusual Electronic and Magnetic Properties*, J. Am. Chem. Soc. **130**, 16739 (2008).

[8] K. Dolui, C. D. Pemmaraju, and S. Sanvito, *Electric Field Effects on Armchair MoS_2 Nanoribbons*, ACS Nano **6**, 4823 (2012).

[9] D. Davelou, G. Kopidakis, E. Kaxiras, and I. N. Remediakis, *Nanoribbon Edges of Transition-Metal Dichalcogenides: Stability and Electronic Properties*, Phys. Rev. B **96**, 165436 (2017).

[10] A. C. Dias, F. Qu, D. L. Azevedo, and J. Fu, *Band Structure of Monolayer Transition-Metal Dichalcogenides and Topological Properties of Their Nanoribbons: Next-Nearest-Neighbor Hopping*, Phys. Rev. B **98**, 075202 (2018).

[11] C. Nethravathi, A. A. Jeffery, M. Rajamathi, N. Kawamoto, R. Tenne, D. Golberg, and Y. Bando, *Chemical Unzipping of WS_2 Nanotubes*, ACS Nano **7**, 7311 (2013).

[12] S. Padmajan Sasikala, Y. Singh, L. Bing, T. Yun, S. H. Koo, Y. Jung, and S. O. Kim, *Longitudinal Unzipping of 2D Transition Metal Dichalcogenides*, Nat Commun **11**, 5032 (2020).

[13] X. Liu, T. Xu, X. Wu, Z. Zhang, J. Yu, H. Qiu, J.-H. Hong, C.-H. Jin, J.-X. Li, X.-R. Wang, et al., *Top–down Fabrication of Sub-Nanometre Semiconducting Nanoribbons Derived from Molybdenum Disulfide Sheets*, Nat Commun **4**, 1 (2013).

[14] J. Wu, H. Zhao, Y. Li, D. Ohlberg, W. Shi, W. Wu, H. Wang, and P. Tan, *Monolayer Molybdenum Disulfide Nanoribbons with High Optical Anisotropy*, Advanced Optical Materials **4**, 756 (2016).

[15] F. Zakerian, M. Fathipour, R. Faez, and G. Darvish, *The Effect of Structural Defects on the Electron Transport of MoS_2 Nanoribbons Based on Density Functional Theory*, J Theor Appl Phys **13**, 55 (2019).

[16] H. E. Lim, Z. Liu, J. Kim, J. Pu, H. Shimizu, T. Endo, Y. Nakanishi, T. Takenobu, and Y. Miyata, *Nanowire-to-Nanoribbon Conversion in Transition-Metal Chalcogenides: Implications for One-Dimensional Electronics and Optoelectronics*, ACS Appl. Nano Mater. acsanm.1c03160 (2021).

[17] F. Cheng, H. Xu, W. Xu, P. Zhou, J. Martin, and K. P. Loh, *Controlled Growth of 1D $MoSe_2$ Nanoribbons with Spatially Modulated Edge States*, Nano Lett. **17**, 1116 (2017).
[18] Y. Chen, P. Cui, X. Ren, C. Zhang, C. Jin, Z. Zhang, and C.-K. Shih, *Fabrication of $MoSe_2$ Nanoribbons via an Unusual Morphological Phase Transition*, Nature Communications **8**, 15135 (2017).
[19] T. Pham, S. Oh, P. Stetz, S. Onishi, C. Kisielowski, M. L. Cohen, and A. Zettl, *Torsional Instability in the Single-Chain Limit of a Transition Metal Trichalcogenide*, Science **361**, 263 (2018).
[20] S. C. Tsang, Y. K. Chen, P. J. F. Harris, and M. L. H. Green, *A Simple Chemical Method of Opening and Filling Carbon Nanotubes*, Nature **372**, 159 (1994).
[21] B. W. Smith, M. Monthioux, and D. E. Luzzi, *Encapsulated C_{60} in Carbon Nanotubes*, Nature **396**, 323 (1998).
[22] E. Philp, J. Sloan, A. I. Kirkland, R. R. Meyer, S. Friedrichs, J. L. Hutchison, and M. L. H. Green, *An Encapsulated Helical One-Dimensional Cobalt Iodide Nanostructure*, Nature Mater **2**, 788 (2003).
[23] C. A. Slade, A. M. Sanchez, and J. Sloan, *Unprecedented New Crystalline Forms of SnSe in Narrow to Medium Diameter Carbon Nanotubes*, Nano Lett. **19**, 2979 (2019).
[24] M. Nagata, S. Shukla, Y. Nakanishi, Z. Liu, Y.-C. Lin, T. Shiga, Y. Nakamura, T. Koyama, H. Kishida, T. Inoue, et al., *Isolation of Single-Wired Transition-Metal Monochalcogenides by Carbon Nanotubes*, Nano Lett. acs.nanolett.8b05074 (2019).
[25] S. Stonemeyer, J. D. Cain, S. Oh, A. Azizi, M. Elasha, M. Thiel, C. Song, P. Ercius, M. L. Cohen, and A. Zettl, *Stabilization of $NbTe_3$, VTe_3, and $TiTe_3$ via Nanotube Encapsulation*, J. Am. Chem. Soc. **143**, 4563 (2021).
[26] S. Stonemeyer, M. Dogan, J. D. Cain, A. Azizi, D. C. Popple, A. Culp, C. Song, P. Ercius, M. L. Cohen, and A. Zettl, *Targeting One- and Two-Dimensional Ta–Te Structures via Nanotube Encapsulation*, Nano Lett. **22**, 2285 (2022).
[27] Z. Wang, H. Li, Z. Liu, Z. Shi, J. Lu, K. Suenaga, S.-K. Joung, T. Okazaki, Z. Gu, J. Zhou, et al., *Mixed Low-Dimensional Nanomaterial: 2D Ultranarrow MoS_2 Inorganic Nanoribbons Encapsulated in Quasi-1D Carbon Nanotubes*, J. Am. Chem. Soc. **132**, 13840 (2010).
[28] Z. Wang, K. Zhao, H. Li, Z. Liu, Z. Shi, J. Lu, K. Suenaga, S.-K. Joung, T. Okazaki, Z. Jin, et al., *Ultra-Narrow WS_2 Nanoribbons Encapsulated in Carbon Nanotubes*, J. Mater. Chem. **21**, 171 (2010).
[29] J. D. Cain, S. Oh, A. Azizi, S. Stonemeyer, M. Dogan, M. Thiel, P. Ercius, M. L. Cohen, and A. Zettl, *Ultranarrow TaS_2 Nanoribbons*, Nano Lett. **21**, 3211 (2021).
[30] See Supplemental Material at [URL Will Be Inserted by Publisher] for methods on synthesis, imaging, simulations and computations, and a movie of the phase change.
[31] L. Rangel DaCosta, H. G. Brown, P. M. Pelz, A. Rakowski, N. Barber, P. O'Donovan, P. McBean, L. Jones, J. Ciston, M. C. Scott, et al., *Prismatic 2.0 – Simulation Software for Scanning and High-Resolution Transmission Electron Microscopy (STEM and HRTEM)*, Micron **151**, 103141 (2021).
[32] J. P. Perdew and A. Zunger, *Self-Interaction Correction to Density-Functional Approximations for Many-Electron Systems*, Phys. Rev. B **23**, 5048 (1981).
[33] P. Giannozzi, S. Baroni, N. Bonini, M. Calandra, R. Car, C. Cavazzoni, D. Ceresoli, G. L. Chiarotti, M. Cococcioni, I. Dabo, et al., *QUANTUM ESPRESSO: A Modular and Open-Source Software Project for Quantum Simulations of Materials*, Journal of Physics: Condensed Matter **21**, 395502 (2009).

[34] D. R. Hamann, *Optimized Norm-Conserving Vanderbilt Pseudopotentials*, Phys. Rev. B **88**, 085117 (2013).
[35] S. Grimme, J. Antony, S. Ehrlich, and H. Krieg, *A Consistent and Accurate Ab Initio Parametrization of Density Functional Dispersion Correction (DFT-D) for the 94 Elements H-Pu*, J. Chem. Phys. **132**, 154104 (2010).
[36] M. L. Cohen, M. Schlüter, J. R. Chelikowsky, and S. G. Louie, *Self-Consistent Pseudopotential Method for Localized Configurations: Molecules*, Phys. Rev. B **12**, 5575 (1975).
[37] José M Soler, Emilio Artacho, Julian D Gale, Alberto García, Javier Junquera, Pablo Ordejón, and Daniel Sánchez-Portal, *The SIESTA Method for Ab Initio Order-N Materials Simulation*, Journal of Physics: Condensed Matter **14**, 2745 (2002).
[38] G. Henkelman, G. Jóhannesson, and H. Jónsson, *Methods for Finding Saddle Points and Minimum Energy Paths*, in *Theoretical Methods in Condensed Phase Chemistry*, edited by S. D. Schwartz (Springer Netherlands, Dordrecht, 2002), pp. 269–302.
[39] G. Henkelman, B. P. Uberuaga, and H. Jónsson, *A Climbing Image Nudged Elastic Band Method for Finding Saddle Points and Minimum Energy Paths*, J. Chem. Phys. **113**, 9901 (2000).
[40] J. Heyd, G. E. Scuseria, and M. Ernzerhof, *Hybrid Functionals Based on a Screened Coulomb Potential*, J. Chem. Phys. **118**, 8207 (2003).
[41] B. I. Yakobson, C. J. Brabec, and J. Bernholc, *Nanomechanics of Carbon Tubes: Instabilities beyond Linear Response*, Phys. Rev. Lett. **76**, 2511 (1996).
[42] J. P. Lu, *Elastic Properties of Carbon Nanotubes and Nanoropes*, Phys. Rev. Lett. **79**, 1297 (1997).
[43] E. Hernández, C. Goze, P. Bernier, and A. Rubio, *Elastic Properties of C and $B_xC_yN_z$ Composite Nanotubes*, Phys. Rev. Lett. **80**, 4502 (1998).
[44] V. N. Popov, V. E. Van Doren, and M. Balkanski, *Elastic Properties of Single-Walled Carbon Nanotubes*, Phys. Rev. B **61**, 3078 (2000).
[45] K. N. Kudin, G. E. Scuseria, and B. I. Yakobson, *C_2F, BN, and C Nanoshell Elasticity from Ab Initio Computations*, Phys. Rev. B **64**, 235406 (2001).
[46] S. Gupta, K. Dharamvir, and V. K. Jindal, *Elastic Moduli of Single-Walled Carbon Nanotubes and Their Ropes*, Phys. Rev. B **72**, 165428 (2005).
[47] L. Wang, D. Liu, F. Zhang, Z. Zhang, J. Cui, Z. Jia, Z. Yu, Y. Lv, and W. Liu, *Dynamics of the Charging-Induced Imaging Instability in Transmission Electron Microscopy*, Nanoscale Adv. **3**, 3035 (2021).
[48] J. Gusakova, X. Wang, L. L. Shiau, A. Krivosheeva, V. Shaposhnikov, V. Borisenko, V. Gusakov, and B. K. Tay, *Electronic Properties of Bulk and Monolayer TMDs: Theoretical Study Within DFT Framework (GVJ-2e Method)*, Physica Status Solidi (a) **214**, 1700218 (2017).
[49] S. Benter, V. G. Dubrovskii, M. Bartmann, A. Campo, I. Zardo, M. Sistani, M. Stöger-Pollach, S. Lancaster, H. Detz, and A. Lugstein, *Quasi One-Dimensional Metal–Semiconductor Heterostructures*, Nano Lett. **19**, 3892 (2019).